

Fermi Large Area Telescope Observations of the Cosmic-Ray Induced γ -ray Emission of the Earth's Atmosphere

A. A. Abdo,^{1,2} M. Ackermann,^{3,*} M. Ajello,³ W. B. Atwood,⁴ L. Baldini,⁵ J. Ballet,⁶ G. Barbiellini,^{7,8} D. Bastieri,^{9,10} B. M. Baughman,¹¹ K. Bechtol,³ R. Bellazzini,⁵ B. Berenji,³ E. D. Bloom,³ E. Bonamente,^{12,13} A. W. Borgland,³ A. Bouvier,³ J. Bregeon,⁵ A. Brez,⁵ M. Brigida,^{14,15} P. Bruel,¹⁶ R. Buehler,³ T. H. Burnett,¹⁷ S. Buson,¹⁰ G. A. Caliendo,¹⁸ R. A. Cameron,³ P. A. Caraveo,¹⁹ J. M. Casandjian,⁶ C. Cecchi,^{12,13} Ö. Çelik,^{20,21,22} E. Charles,³ A. Chekhtman,^{1,23} J. Chiang,³ S. Ciprini,¹³ R. Claus,³ J. Cohen-Tanugi,²⁴ J. Conrad,^{25,26,27} F. de Palma,^{14,15} S. W. Digel,³ E. do Couto e Silva,³ P. S. Drell,³ R. Dubois,³ D. Dumora,^{28,29} C. Farnier,²⁴ C. Favuzzi,^{14,15} S. J. Fegan,¹⁶ W. B. Focke,³ P. Fortin,¹⁶ M. Frailis,³⁰ Y. Fukazawa,³¹ S. Funk,^{3,†} P. Fusco,^{14,15} F. Gargano,¹⁵ N. Gehrels,^{20,32,33} S. Germani,^{12,13} B. Giebels,¹⁶ N. Giglietto,^{14,15} F. Giordano,^{14,15} T. Glanzman,³ G. Godfrey,³ I. A. Grenier,⁶ M.-H. Grondin,^{28,29} J. E. Grove,¹ L. Guillemot,³⁴ S. Guiriec,³⁵ E. Hays,²⁰ D. Horan,¹⁶ R. E. Hughes,¹¹ G. Jóhannesson,³ A. S. Johnson,³ T. J. Johnson,^{20,33} W. N. Johnson,¹ T. Kamae,³ H. Katagiri,³¹ J. Kataoka,³⁶ N. Kawai,^{37,38} M. Kerr,¹⁷ J. Knödlseeder,³⁹ M. Kuss,⁵ J. Lande,³ L. Latronico,⁵ M. Lemoine-Goumard,^{28,29} F. Longo,^{7,8} F. Loparco,^{14,15} B. Lott,^{28,29} M. N. Lovellette,¹ P. Lubrano,^{12,13} A. Makeev,^{1,23} M. N. Mazziotta,¹⁵ J. E. McEnery,^{20,33} C. Meurer,^{25,26} P. F. Michelson,³ W. Mitthumsiri,^{3,‡} T. Mizuno,³¹ C. Monte,^{14,15} M. E. Monzani,³ A. Morselli,⁴⁰ I. V. Moskalenko,³ S. Murgia,³ P. L. Nolan,³ J. P. Norris,⁴¹ E. Nuss,²⁴ T. Ohsugi,³¹ A. Okumura,⁴² N. Omodei,⁵ E. Orlando,⁴³ J. F. Ormes,⁴¹ D. Paneque,³ J. H. Panetta,³ D. Parent,^{28,29} V. Pelassa,²⁴ M. Pepe,^{12,13} M. Pesce-Rollins,⁵ F. Piron,²⁴ T. A. Porter,⁴ S. Rainò,^{14,15} R. Rando,^{9,10} M. Razzano,⁵ A. Reimer,^{44,3} O. Reimer,^{44,3} T. Reposeur,^{28,29} L. S. Rochester,³ A. Y. Rodriguez,¹⁸ M. Roth,¹⁷ H. F.-W. Sadrozinski,⁴ A. Sander,¹¹ P. M. Saz Parkinson,⁴ C. Sgrò,⁵ G. H. Share,^{1,45} E. J. Siskind,⁴⁶ D. A. Smith,^{28,29} P. D. Smith,¹¹ G. Spandre,⁵ P. Spinelli,^{14,15} M. S. Strickman,¹ D. J. Suson,⁴⁷ H. Takahashi,³¹ T. Tanaka,³ J. B. Thayer,³ J. G. Thayer,³ D. J. Thompson,²⁰ L. Tibaldo,^{9,10,6} D. F. Torres,^{48,18} G. Tosti,^{12,13} A. Tramacere,^{3,49} Y. Uchiyama,³ T. L. Usher,³ V. Vasileiou,^{21,22} N. Vilchez,³⁹ V. Vitale,^{40,50} A. P. Waite,³ P. Wang,³ B. L. Winer,¹¹ K. S. Wood,¹ T. Ylinen,^{51,52,26} and M. Ziegler⁴

(Fermi-LAT collaboration)

¹Space Science Division, Naval Research Laboratory, Washington, DC 20375, USA

²National Research Council Research Associate, National Academy of Sciences, Washington, DC 20001, USA

³W. W. Hansen Experimental Physics Laboratory,

Kavli Institute for Particle Astrophysics and Cosmology,

Department of Physics and SLAC National Accelerator Laboratory, Stanford University, Stanford, CA 94305, USA

⁴Santa Cruz Institute for Particle Physics, Department of Physics and Department of Astronomy and Astrophysics, University of California at Santa Cruz, Santa Cruz, CA 95064, USA

⁵Istituto Nazionale di Fisica Nucleare, Sezione di Pisa, I-56127 Pisa, Italy

⁶Laboratoire AIM, CEA-IRFU/CNRS/Université Paris Diderot, Service d'Astrophysique, CEA Saclay, 91191 Gif sur Yvette, France

⁷Istituto Nazionale di Fisica Nucleare, Sezione di Trieste, I-34127 Trieste, Italy

⁸Dipartimento di Fisica, Università di Trieste, I-34127 Trieste, Italy

⁹Istituto Nazionale di Fisica Nucleare, Sezione di Padova, I-35131 Padova, Italy

¹⁰Dipartimento di Fisica "G. Galilei", Università di Padova, I-35131 Padova, Italy

¹¹Department of Physics, Center for Cosmology and Astro-Particle Physics, The Ohio State University, Columbus, OH 43210, USA

¹²Istituto Nazionale di Fisica Nucleare, Sezione di Perugia, I-06123 Perugia, Italy

¹³Dipartimento di Fisica, Università degli Studi di Perugia, I-06123 Perugia, Italy

¹⁴Dipartimento di Fisica "M. Merlin" dell'Università e del Politecnico di Bari, I-70126 Bari, Italy

¹⁵Istituto Nazionale di Fisica Nucleare, Sezione di Bari, 70126 Bari, Italy

¹⁶Laboratoire Leprince-Ringuet, École polytechnique, CNRS/IN2P3, Palaiseau, France

¹⁷Department of Physics, University of Washington, Seattle, WA 98195-1560, USA

¹⁸Institut de Ciències de l'Espai (IEEC-CSIC), Campus UAB, 08193 Barcelona, Spain

¹⁹INAF-Istituto di Astrofisica Spaziale e Fisica Cosmica, I-20133 Milano, Italy

²⁰NASA Goddard Space Flight Center, Greenbelt, MD 20771, USA

²¹Center for Research and Exploration in Space Science and Technology

(CRESST) and NASA Goddard Space Flight Center, Greenbelt, MD 20771, USA

²²Department of Physics and Center for Space Sciences and Technology, University of Maryland Baltimore County, Baltimore, MD 21250, USA

²³George Mason University, Fairfax, VA 22030, USA

²⁴Laboratoire de Physique Théorique et Astroparticules, Université Montpellier 2, CNRS/IN2P3, Montpellier, France

- ²⁵Department of Physics, Stockholm University, AlbaNova, SE-106 91 Stockholm, Sweden
- ²⁶The Oskar Klein Centre for Cosmoparticle Physics, AlbaNova, SE-106 91 Stockholm, Sweden
- ²⁷Royal Swedish Academy of Sciences Research Fellow,
funded by a grant from the K. A. Wallenberg Foundation
- ²⁸Université de Bordeaux, Centre d'Études Nucléaires Bordeaux Gradignan, UMR 5797, Gradignan, 33175, France
- ²⁹CNRS/IN2P3, Centre d'Études Nucléaires Bordeaux Gradignan, UMR 5797, Gradignan, 33175, France
- ³⁰Dipartimento di Fisica, Università di Udine and Istituto Nazionale di Fisica Nucleare,
Sezione di Trieste, Gruppo Collegato di Udine, I-33100 Udine, Italy
- ³¹Department of Physical Sciences, Hiroshima University, Higashi-Hiroshima, Hiroshima 739-8526, Japan
- ³²Department of Astronomy and Astrophysics, Pennsylvania State University, University Park, PA 16802, USA
- ³³Department of Physics and Department of Astronomy,
University of Maryland, College Park, MD 20742, USA
- ³⁴Max-Planck-Institut für Radioastronomie, Auf dem Hügel 69, 53121 Bonn, Germany
- ³⁵Center for Space Plasma and Aeronomic Research (CSPAR),
University of Alabama in Huntsville, Huntsville, AL 35899, USA
- ³⁶Waseda University, 1-104 Totsukamachi, Shinjuku-ku, Tokyo, 169-8050, Japan
- ³⁷Department of Physics, Tokyo Institute of Technology, Meguro City, Tokyo 152-8551, Japan
- ³⁸Cosmic Radiation Laboratory, Institute of Physical and Chemical Research (RIKEN), Wako, Saitama 351-0198, Japan
- ³⁹Centre d'Étude Spatiale des Rayonnements, CNRS/UPS, BP 44346, F-30128 Toulouse Cedex 4, France
- ⁴⁰Istituto Nazionale di Fisica Nucleare, Sezione di Roma "Tor Vergata", I-00133 Roma, Italy
- ⁴¹Department of Physics and Astronomy, University of Denver, Denver, CO 80208, USA
- ⁴²Department of Physics, Graduate School of Science,
University of Tokyo, 7-3-1 Hongo, Bunkyo-ku, Tokyo 113-0033, Japan
- ⁴³Max-Planck Institut für extraterrestrische Physik, 85748 Garching, Germany
- ⁴⁴Institut für Astro- und Teilchenphysik and Institut für Theoretische Physik,
Leopold-Franzens-Universität Innsbruck, A-6020 Innsbruck, Austria
- ⁴⁵Praxis Inc., Alexandria, VA 22303, USA
- ⁴⁶NYCB Real-Time Computing Inc., Lattingtown, NY 11560-1025, USA
- ⁴⁷Department of Chemistry and Physics, Purdue University Calumet, Hammond, IN 46323-2094, USA
- ⁴⁸Institució Catalana de Recerca i Estudis Avançats (ICREA), Barcelona, Spain
- ⁴⁹Consorzio Interuniversitario per la Fisica Spaziale (CIFS), I-10133 Torino, Italy
- ⁵⁰Dipartimento di Fisica, Università di Roma "Tor Vergata", I-00133 Roma, Italy
- ⁵¹Department of Physics, Royal Institute of Technology (KTH), AlbaNova, SE-106 91 Stockholm, Sweden
- ⁵²School of Pure and Applied Natural Sciences, University of Kalmar, SE-391 82 Kalmar, Sweden

(Dated: October 26, 2018)

We report on measurements of the cosmic-ray induced γ -ray emission of Earth's atmosphere by the Large Area Telescope onboard the *Fermi* Gamma-ray Space Telescope. The LAT has observed the Earth during its commissioning phase and with a dedicated Earth-limb following observation in September 2008. These measurements yielded $\sim 6.4 \times 10^6$ photons with energies > 100 MeV and ~ 250 hours total livetime for the highest quality data selection. This allows the study of the spatial and spectral distributions of these photons with unprecedented detail. The spectrum of the emission – often referred to as Earth albedo gamma-ray emission – has a power-law shape up to 500 GeV with spectral index $\Gamma = 2.79 \pm 0.06$.

I. INTRODUCTION

For an earth-orbiting γ -ray detector such as the Large Area Telescope (LAT) on board the Fermi γ -ray Space Telescope (*Fermi*), the Earth is the brightest source in the sky due to its proximity. The γ -ray emission from the Earth is produced by cosmic-ray interactions with the Earth's atmosphere, and is often called the γ -ray albedo. The vast majority of cosmic rays are protons and heavier nuclei. Atmospheric γ -ray emission is the result of cosmic-ray cascades, mainly through the decay of neutral pions and kaons and through Bremsstrahlung of electrons and positrons (dominating at energies below ~ 50 MeV [1]). Due to the kinematics of the collisions, the cross sections of these processes at high energies are peaked in the forward direction.

*Electronic address: markusa@slac.stanford.edu

†Electronic address: funk@slac.stanford.edu

‡Electronic address: warit@slac.stanford.edu

The spectrum of the albedo γ -rays is not uniform across the Earth's disk. The spectrum of the inner part of the disk is soft owing to the small number of secondary particles, typically neutral pions, that are back-scattered at large angles relative to the direction of the cosmic-ray cascade developing deep into the atmosphere. Cosmic rays that enter the atmosphere near grazing incidence produce showers whose forward-moving γ -rays can penetrate the thin atmospheric layer making the limb bright when viewed from orbit. The geometric effect of shower production and absorption in the atmosphere producing a bright γ -ray horizon was first calculated by Stecker [2]. A Monte Carlo model of γ -ray production by cosmic-ray interactions in the atmosphere later developed by Morris [1] produced reasonable agreement with the spatial and spectral measurements by various balloon-borne and spacecraft instruments.

The Earth's γ -ray emission has been observed by several previous satellite missions starting as early as the 1960s with a detector flown on the third Orbiting Solar Observatory, *OSO-3*, for energies above 50 MeV [3]. This instrument detected an enhancement of γ -rays when pointing towards the Earth, consistent with balloon flight measurements [4, 5, 6, 7, 8] and followed up by other satellite missions [9, 10, 11, 12]. A more detailed study of the γ -ray emission from interactions of cosmic rays with the Earth's atmosphere was done by Thompson et al. [13] using approximately 6700 γ -ray events from the Earth, recorded with the second Small Astronomy Satellite, *SAS-2*. These early measurements showed a clear peak of γ -ray intensity towards the Earth horizon, with a factor of ~ 10 larger intensity than seen towards the nadir direction. Also they show a modulation of the γ -ray intensity with respect to the east-west direction as expected from the deflection of cosmic rays in the Earth's magnetic field. These findings were confirmed and extended to higher energies with the high-energy γ -ray satellite detector on-board the *Compton Gamma-Ray Observatory (CGRO)*, the Energetic γ -ray Experiment Telescope (EGRET). EGRET was in operation from 1991 to 2000, and approximately 60% of the mission's total 5.2 million events were measured from the Earth direction [14].

The next generation γ -ray observatory, *Fermi*, was launched on 11 June 2008. The primary instrument on *Fermi*, the Large Area Telescope (LAT), is a pair-conversion telescope that detects γ -rays through conversion into an e^+e^- pair. The trajectories of this pair are recorded in the tracker and allows for the reconstruction of the direction of the incident photon. The subsequent particle shower development is sampled in the tracker and a calorimeter to determine the photon energy. The LAT's wide field of view (~ 2.4 sr), effective area (~ 8000 cm² at 1 GeV), improved point spread function (PSF), and broad energy coverage (20 MeV to > 300 GeV) provide significantly improved sensitivity over its predecessors [15].

During routine science operations (the so-called "survey" mode), the LAT points away from the Earth because of the relative brightness of the Earth at GeV γ -ray energies and the background it would introduce to astrophysical sources. The center of the field-of-view (z -axis) of the LAT is kept within 35° relative to the zenith (the direction pointing away from the center of the Earth) for most of the time¹. However, during the commissioning phase of the instrument, the pointing was such that parts of the Earth were within the field-of-view at varying angles with respect to the LAT z -axis. In addition, during September 2008 a dedicated observation of the Earth's limb was made. This combined dataset can be used for the analysis of the albedo emission.

There are several reasons that render a study of the Earth's γ -ray albedo with the LAT useful. First, measurements of the albedo γ -rays contribute to the understanding of the celestial γ -ray background for the LAT and future satellite instruments. Second, such observations can be used for a calibration of the LAT instrument. Finally, if the production of secondary γ -rays in the Earth's atmosphere is sufficiently well understood and modeled, observations of the albedo emission yield a measurement of the interactions of primary cosmic rays with the Earth's atmosphere and can, therefore, provide information on the spectrum of primary cosmic rays, interaction cross sections, atmospheric properties, and the deflection of primary cosmic rays by the geomagnetic field.

The current work describes the analysis of the Earth's γ -rays albedo emission at energies above 100 MeV observed with the LAT.

II. DATASET

Two main data sets have been used: (i) the Launch & Early Operations (LEO) data taken during the first 60 days of the mission, during which time the Earth limb was often closer to the field of view than during a regular sky survey (only data were used that were suitable for science observations), (ii) two orbits (i.e. close to 3 hours) of direct limb observations during which the Earth limb was kept within the field of view with the aim of adding on-axis photons to the overall data set. The LEO data contain many different observation modes, but the main modes are a north-orbital-pole pointing and a pointing mode with the LAT z -axis centered at the Vela pulsar. All results shown here are averaged over many orbits of *Fermi* and correspond to the highest quality event selection currently available

¹ This rocking angle has recently been increased to 50°

for the LAT data (the so-called “diffuse” class events [15]). The total number of events > 100 MeV in our dataset is $\sim 6.4 \times 10^6$ corresponding to ~ 250 hours of livetime. The maximum total exposure is close to the Earth north pole with $\sim 2 \times 10^9$ cm² s at 1 GeV.

In addition to the standard diffuse cuts, corresponding to the post-launch instrument response functions *P6V3*, we applied the following selections:

- $\Theta_{\text{nadir}} < 80^\circ$ to select photons coming from the earth.
- $\Theta_{\text{LAT}} < 65^\circ$ to avoid the edge of the field of view of the LAT (Θ_{LAT} being the angle with respect to the LAT z-axis).

III. RESULTS

A. Intensity Maps

To generate intensity maps we transform the incident photon directions into the Earth-centric coordinate system with angles Θ_{nadir} and Φ_{nadir} denoting the zenithal and azimuthal angle about the direction pointing from the spacecraft towards the center of the Earth, where $\Phi_{\text{nadir}} = 0$ corresponds to the north. The photons were binned in solid angle for energy intervals with spacing 10 bins per decade from 200 MeV up to 500 GeV. The solid angle bins were spaced equally in 5° bins in Φ_{nadir} with an energy dependent binning in Θ_{nadir} changing from 1° at 200 MeV to 0.1° above 10 GeV to take into account the LAT’s energy-dependent angular resolution. The LAT pointing and livetime history were evaluated in the same coordinate system in 30-second time steps, creating maps of the exposure of the spacecraft to allow conversion from photon counts per solid angle to intensities.

Figure 1 shows the resulting exposure and photon intensity maps for 3 different energy bands (left: 200 MeV to 1 GeV, center: 1 GeV to 10 GeV, right: 10 GeV to 500 GeV). The center of each plot (i.e. $\Theta_{\text{nadir}} = 0^\circ$) is the nadir direction, while the edge of the plots are the horizon at LAT’s altitude ($\Theta_{\text{nadir}} = 90^\circ$). North is to the top of the maps and west to the left. All intensity maps have been background corrected by subtracting the average intensity from a ring between $\Theta_{\text{nadir}} = 79^\circ$ to 80° averaged over Φ_{nadir} .

The exposure is a factor ~ 2 higher in the north compared to south (top row). This is due to the observation strategy in which the majority of the data were taken during a north-orbital pole pointing. The exposure increases with energy due to the increase in the LAT effective area. It can also be seen that towards the nadir the exposure is much lower than towards the rim. To avoid the introduction of large errors from low exposure bins in the spectral analysis, areas where the exposure is less than 0.5% of the maximum exposure in the corresponding energy band are excluded from the analysis in all energy bands. The discarded areas due to low exposure match the black regions in the center of the exposure maps. Compared with EGRET, the LAT exposure is about a factor of ~ 30 larger [14].

The γ -ray intensity maps (bottom row) in units of photons cm⁻² s⁻¹ sr⁻¹ show the bright limb of the Earth, with the emission becoming less intense toward nadir. The Earth limb is very bright with intensities of up to 0.01 photons cm⁻² s⁻¹ sr⁻¹ in the low energy bands – more than one order of magnitude brighter than the center of the Galaxy for the same energy range. The narrowing of the emission with increasing energy is an effect of both the PSF of the LAT improving at higher energies [15] and the increasing contribution by γ -rays produced in the forward direction of the cosmic-ray showering at higher energies. Only 27 photons above 10 GeV are detected with angles $\Theta_{\text{nadir}} < 60^\circ$. The maximum of the γ -ray emission is detected from a narrow region at $\Theta_{\text{nadir}} \sim 68^\circ$. The intensity maps also show significant modulation between east and west with the effect decreasing as the γ -ray energy increases (this is the so-called “east-west effect”). Photons arriving from directions excluded from the analysis due to low exposure are not shown on the maps.

Our measurements are in a good qualitative agreement with expectations from standard cosmic-ray air-shower phenomenology.

The east-west effect that can be seen in the lower energy intensity maps is due to the deflection of cosmic rays in the Earth’s magnetic field. If there was no magnetic field the cosmic ray intensities at the top of the atmosphere would be isotropic, and no east-west asymmetry would exist. However, the presence of the magnetic field biases the cosmic-ray intensities interacting in the atmosphere. There are fewer cosmic rays interacting from an easterly direction than the west because the magnetic field disallows trajectories from the east. This effect is energy dependent so that low-energy cosmic rays are affected more than high-energy cosmic rays (those with energies above ~ 50 GeV are unaffected). Since the majority of the emission near the limb comes from viewing the development of the cosmic-ray showers in the forward direction, the reduced cosmic-ray intensity from the east effectively suppresses the shower products coming from this direction. This effect vanishes when the atmospheric photons are predominantly generated by cosmic rays that have large enough energies to allow them to reach the atmosphere undeflected by Earth’s magnetic field. This is the case for secondary photons with energies $\gtrsim 10$ GeV.

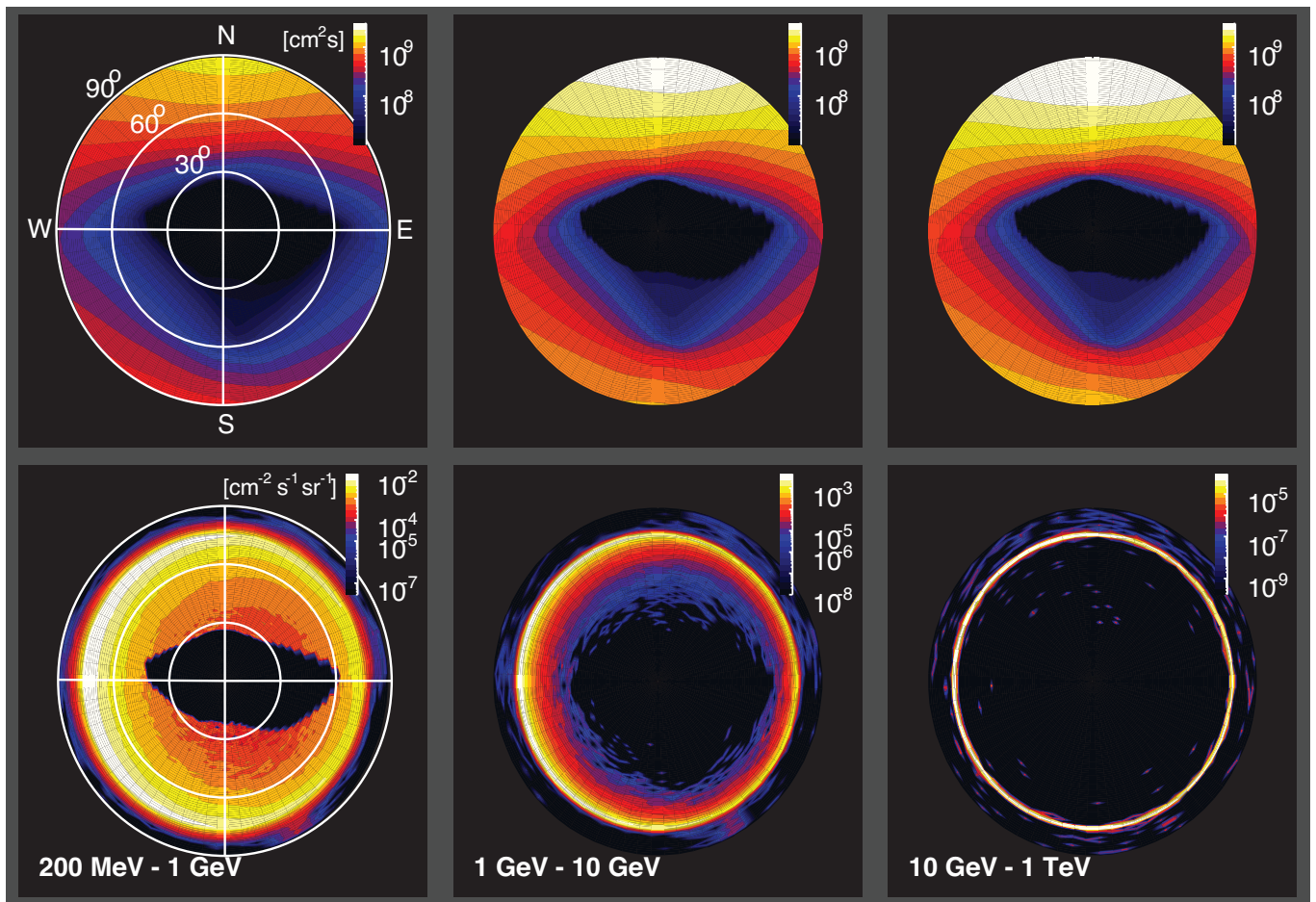


FIG. 1: Two-dimensional maps of exposure (top row) and intensity (bottom row) for three different energy bands. The coordinate system in these maps is a polar representation such that the nadir-direction (i.e. looking down towards the center of the Earth) with $\Theta_{\text{nadir}} = 0^\circ$ is at the center of the plot. Θ_{nadir} is increasing in radial direction with the edge of the plot towards the horizon at $\Theta_{\text{nadir}} = 90^\circ$. The north pole is to the top and west is to the left. The exposure maps are given in units of $\text{cm}^2 \text{s}$, the intensity maps in units of $\text{cm}^{-2} \text{s}^{-1} \text{sr}^{-1}$.

The high-energy γ -rays ($E_\gamma > 10 \text{ GeV}$) are concentrated in a very narrow band toward, but not exactly aligned with, the Earth-limb angle, which is at 66.7° for the LAT's orbital altitude of 565 km. At these high energies the number of back-scattered γ -rays formed in the shower development is negligible and the intensity is dominated by forward-emitted γ -rays from incident cosmic rays with tangential directions to the Earth's surface. Vertically incident showers have their first interaction in the range between 10–20 km, which corresponds to $\Theta_{\text{nadir}} \sim 67^\circ$. The atmospheric column density in the limb direction is large, being many attenuation lengths of material, which suppresses the γ -ray emission close to the limb. In addition, the LAT views mostly grazing-incidence cosmic rays in the higher parts of the atmosphere. Therefore the maximum of the emission is in the range between $\Theta_{\text{nadir}} = 67^\circ$ to 69° . For zenith angles larger than about $\Theta_{\text{nadir}} = 70^\circ$ the atmospheric depth left to produce a hadronic shower becomes too low and, therefore, very few γ -rays are detected. For zenith-angles smaller than the limb angle at $\Theta_{\text{nadir}} \sim 66.7^\circ$, the Earth and its atmosphere form an opaque barrier to forward-emitted γ -rays. Only the significantly lower-intensity back-scattered and off-axis emission from the cosmic-ray shower development is detected for these viewing angles. Thus, the maps above 10 GeV show a very narrow band close to but not at the Earth's limb.

B. Spectrum

Figure 2 shows the LAT-measured energy spectrum of the atmospheric γ -rays for different nadir bands integrated over azimuth angles. The spectra have been corrected for spill-over effects due to the LAT PSF. This was done by measuring the intensity in each energy bin outside of the Earth limb, where very little emission is expected due to

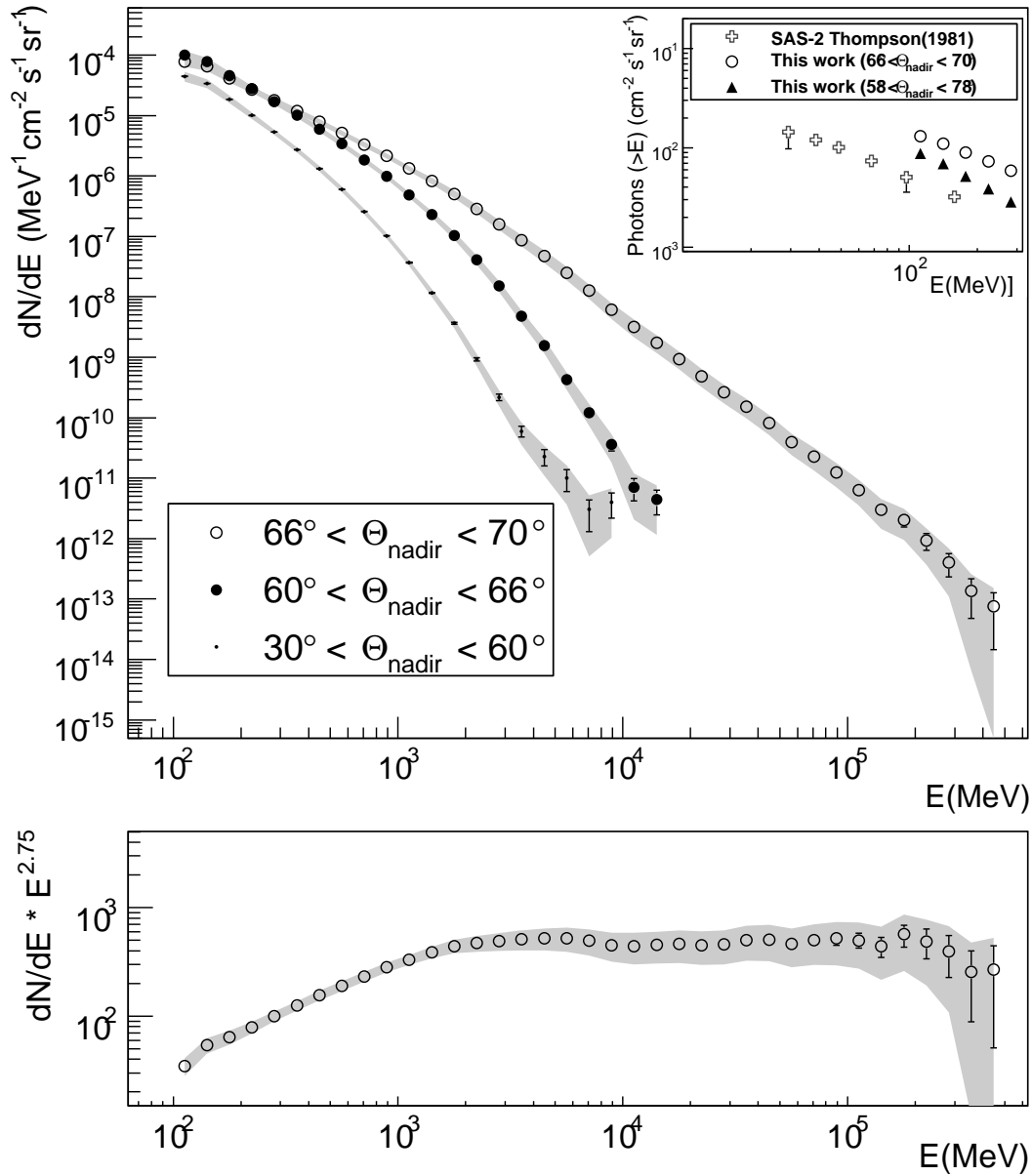


FIG. 2: Differential energy spectrum for the γ -rays produced in the Earth's atmosphere taken in different Θ_{nadir} -bands. The spectrum of the limb (open circles) shows a power-law behavior. Also shown are γ -ray spectra for the inner parts of the Earth's disk (filled circles and points). Indicated are both statistical and systematic errors (grey band), the latter derived from studies of the Vela pulsar. The inset shows a comparison to previous data by the *SAS-2* satellite [13]. To allow for a direction comparison, the limb-spectrum is also shown for a larger integration region ($58^\circ < \Theta_{\text{nadir}} < 78^\circ$) corresponding to the *SAS-2* measurement. The bottom panel shows the limb-spectrum multiplied by energy to the power 2.75.

the significantly lower atmospheric density. Outside of the rim is defined here as $70^\circ < \Theta_{\text{nadir}} < 73^\circ$. Only for the low energy part of the spectrum (below ~ 1.5 GeV) this spill-over effect is relevant. Beyond that energy the intensity outside the rim is lower by many orders of magnitude than the intensity from inside the rim.

The average differential spectrum of the limb region (open circles), i.e. for $66^\circ < \Theta_{\text{nadir}} < 70^\circ$, shows evidence for a turn-over at energies below 3 GeV. Between 3 GeV and 500 GeV the spectrum can be fitted with a power-law $dN/dE = I_0 E^{-\Gamma}$ with normalization $I_0 = (7.4 \pm 1.0) \times 10^2 \text{ MeV}^{-1} \text{ cm}^{-2} \text{ s}^{-1} \text{ sr}^{-1}$ and photon index $\Gamma = 2.79 \pm 0.06$. Since both the intensity and the exposure vary considerably over the limb region, a derivation of the statistical errors is not straightforward. To determine the statistical errors we use a Monte Carlo technique: 1000 pseudo-count experiments are generated for each energy bin, using the LAT exposure and a model of the gamma-ray intensity emitted by the Earth albedo derived from EGRET observations [14]. In this model, the average intensity from the

limb is renormalized to match the intensities reported here. The RMS of the intensities derived from these pseudo-experiments is then used as the uncertainty of the reported gamma-ray intensity from the Earth limb.

For the fit, the systematic errors (shown as grey band) have been taken into account, conservatively adding them linearly to the statistical errors. These systematic errors have been derived from Vela observations by comparing the measured γ -rays to various simulation of γ -rays from Vela where these simulations take the uncertainties in the instrument response functions into account [16]. These systematic errors therefore essentially show the contribution from the uncertainties in the effective area of the instrument. For energies above 10 GeV, the systematic errors are less well known (due to the Vela cutoff) and have been extrapolated from the value at 10 GeV. For this high-statistics data set, the systematic errors dominate over the statistical errors nearly up to the highest energies.

The bottom panel of Fig. 2 shows the differential intensity multiplied by $E^{2.75}$ – the spectral index of cosmic-ray protons [17, 18]. The χ^2 of the fit is 1.2 for 19 degrees of freedom when using the systematic errors in the fitting ($\chi^2/\text{ndf} = 89/19$ when using only statistical errors).

The integrated intensity of Earth's limb above 100 MeV is $5.2 \times 10^{-3} \text{ cm}^{-2} \text{ s}^{-1} \text{ sr}^{-1}$, which makes the Earth by far the single brightest source in the LAT energy range. For this data set there are 16 photons above 500 GeV and 3 events above 1 TeV with the highest energy photon having an energy of 1.14 TeV. Events above 500 GeV have not been used in the spectral analysis since the energy calibration of the LAT is still under investigation at these energies. Also shown as solid circles and dots are the spectra for two inner regions of the Earth's disk ($60^\circ < \Theta_{\text{nadir}} < 66^\circ$ and $30^\circ < \Theta_{\text{nadir}} < 60^\circ$). The spectra become much softer above a few hundred MeV when moving towards the inner part of the disk. Fitting the inner parts by a power-law with energy-dependent index of the form $dN/dE = I_0 E^{-\Gamma - \beta \log_{10}(E/\text{MeV})}$ yields $\Gamma = 7.76 \pm 3.1$ and $\beta = 1.78 \pm 0.5$ for the range between $60^\circ < \Theta_{\text{nadir}} < 66^\circ$ and $\Gamma = 6.9 \pm 0.1$ and $\beta = 1.90 \pm 0.02$ for the range between $30^\circ < \Theta_{\text{nadir}} < 66^\circ$.

The spectrum of the Earth's limb is dominated by γ -rays from cosmic ray interactions in the upper atmospheric layers (in tangential directions) pointed towards the LAT that do not suffer large energy losses in the atmosphere (as compared to the back-scattered γ -rays). At high γ -ray energies (above 3.2 GeV) the spectrum enters the regime of cosmic-ray primaries ($\gtrsim 10$ GeV) unaffected by the Earth's magnetic fields, and, therefore, should have a spectral index close to that of cosmic rays [19]. The fitted power-law index of the atmospheric γ -ray emission from the limb is $\Gamma = 2.79 \pm 0.05$, compared to an index of $\Gamma = 2.75 \pm 0.03$ for the primary cosmic-ray spectrum. Since the spectrum of cosmic rays is well measured, eventually, the γ -rays from the Earth's atmosphere might help to calibrate the effective area of the LAT beyond the energy regime where we have test-beam data. As previously described, moving from the limb to the inner regions of the Earth, the LAT moves from measuring the CR showers from a predominantly forward direction to a side-on view and then to a backward direction. This results in a much steeper spectrum for the inner parts with very few γ -rays above 1 GeV as shown by the filled circles.

The inset in the top panel of Fig. 2 shows a comparison with previous results as published in Thompson et al. [13]. The spectra are qualitatively similar when taking into account the region for which the *SAS-2* spectrum had been derived ($\pm 10^\circ$ around the Earth limb). The differences in the measured flux could be due to the limited energy resolution of *SAS-2* or the fact that when the PSF is folded into the integration region, the match in areas over which the measurements were taken is not perfect.

C. Azimuthal and Zenithal profiles

Figure 3 shows an azimuthal profile of the limb emission (i.e. for $60^\circ < \Theta_{\text{nadir}} < 75^\circ$) for four different energy bands (0.2-1 GeV, 1-10 GeV, 10-30 GeV and above 30 GeV). As can be seen, the east-west effect is a very prominent modulation at low energies with a factor of ~ 5 intensity difference between the minimum in the east (at $\Phi_{\text{nadir}} = 90^\circ$) and the maximum in the west (at $\Phi_{\text{nadir}} = 270^\circ$). This factor is consistent with what has been shown for EGRET data [14]. The difference in intensity between the east and the west for the highest energy band is consistent within errors with no modulation ($(8.0 \pm 2.0) \times 10^{-7} \text{ cm}^{-2} \text{ s}^{-1} \text{ sr}^{-1}$ from the east and $(10.0 \pm 2.0) \times 10^{-7} \text{ cm}^{-2} \text{ s}^{-1} \text{ sr}^{-1}$ from the west). The no-modulation hypothesis provides an acceptable fit only for the > 30 GeV band ($\chi^2 = 74$ for 71 degrees of freedom). All other bands show the variation in intensity with azimuth and hence a poor fit to a constant (for example, the 10 – 30 GeV band has a $\chi^2 = 188$ for 71 degrees of freedom). A comparison between the intensity from the north and the intensity from the south is consistent within errors (variation is below 15%). The behavior of these azimuthal variations can be qualitatively understood taking into account the production mechanism. Low-energy cosmic-ray shower products are altered by Earth's magnetic field and due to their predominantly positive charge preferentially selects particles coming from the west. Higher-energy cosmic rays have higher magnetic rigidities and are therefore less affected by Earth's magnetic field.

Fig. 4 shows the zenith angle distribution for several energy bands separated into angular segments of 90° referenced to the nadir centred on the directions north, east, south, and west. These plots have been background subtracted by taking the average intensity in the wedge at $\Theta_{\text{nadir}} = 80^\circ$ (beyond the Earth's disk) as a background estimation. For

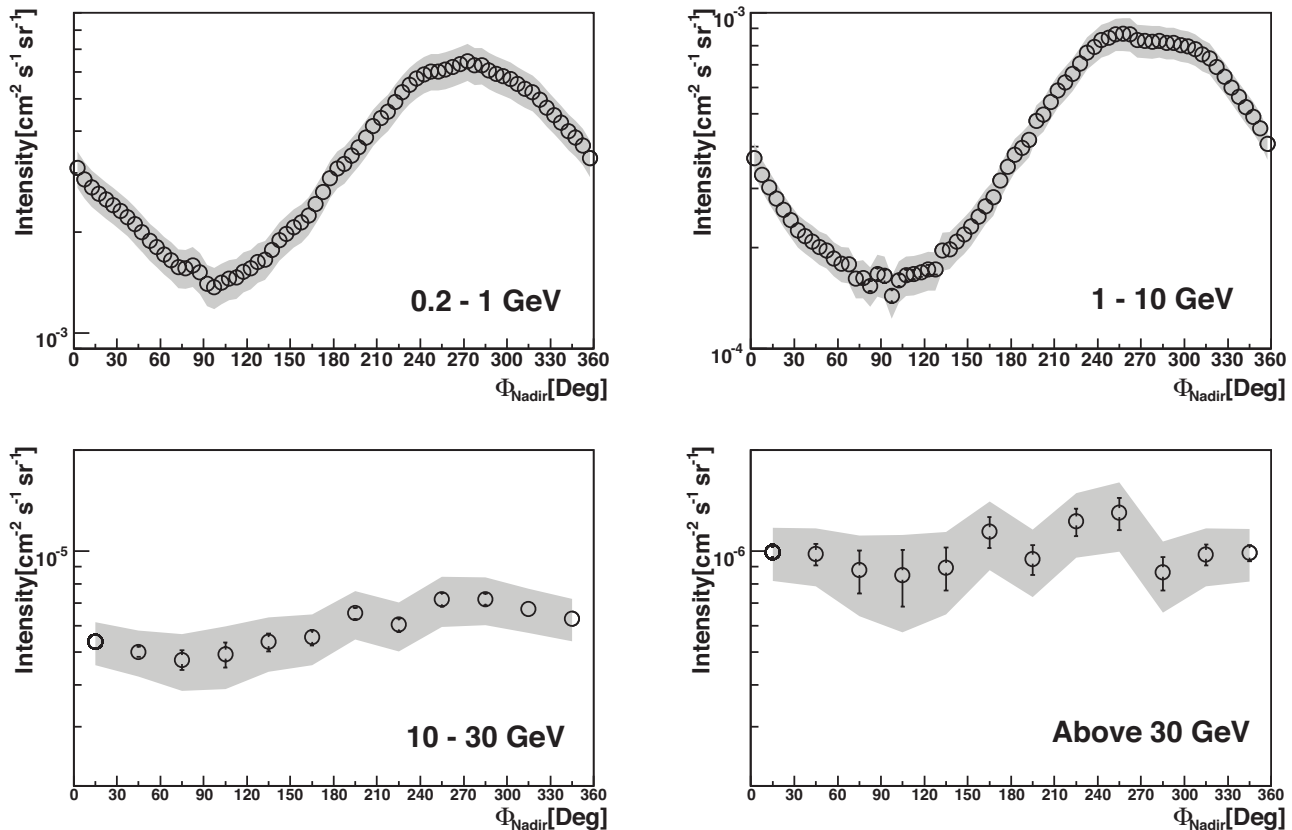


FIG. 3: Photon intensity as a function of azimuth for 4 different energy bands along the limb ($60^\circ < \Theta_{\text{nadir}} < 75^\circ$). Systematic errors as derived from LAT data on the Vela pulsar are shown as grey bands. A modulation is apparent in the low-energy bands which fades away at higher energies (see text for more details).

comparison the dashed line shows the LAT PSF (averaged between front and back-converting events) calculated for the lower bound of the energy bin (the low energy photons dominate the emission in each of the energy bins). Note that for the two higher-energy bins the range and the bin size of these histograms have been reduced to feature the limb emission. As can be seen, the Earth emission is wider than the LAT PSF even for the highest band, in which the LAT PSF is better than 0.1° (68% containment radius). The good agreement in intensity from north and south can be seen in this figure which provides a systematic check on the true nature of the east-west effect.

The angular distribution of photons near the rim can be used to compare the γ -ray emission with a simple atmospheric model to investigate the effect of the absorption of γ -rays. The proton-air interaction length is $X_i \sim 85 \text{ g cm}^{-2}$, which can be estimated using the value $\sim 275 \text{ mb}$ for the total inelastic $p^{14}\text{N}$ cross section [20]. In the thin target regime, when the atmospheric depth is $X \ll X_i$, the intensity of produced γ -rays is $\propto X$. A competing process is the attenuation of γ -rays due to the e^+e^- -pair production, with the corresponding scale, the radiation length, of $X_0 \sim 38 \text{ g cm}^{-2}$ in the atmosphere [21]. The interplay between these processes sets the value of column density when the effect of absorption of γ -rays becomes noticeable $\gtrsim 10 \text{ g cm}^{-2}$.

Indeed, this behavior is demonstrated in Figure 5, which shows the integrated atmospheric column depth along the line of sight for a given nadir angle at a height 560 km for two different atmospheric models. The solid line shows the curve for a simple model of the atmosphere with an exponential density profile with scale height 6.8 km [22] following the *barometer formula* $X(h) = X(h=0)e^{-(h/h_s)}$ with $X(h)$ in units of g cm^{-2} denoting the column density of air overlaying a point at altitude h in cm. The dashed line shows a more realistic atmospheric model (NRLMSISE-00) as given by Picone et al. [23]. Overlaid on the atmospheric column densities is the γ -ray intensity (scaled to match the barometric atmosphere profile) averaged over all theta angles (solid circles). Also shown is the deconvolved LAT intensity (open circles) in these angles for the PSF at the median energy of this data set (4.7 GeV). The plot shows, that far enough out beyond the rim (in the plot for angles $\Theta_{\text{nadir}} > 68.3^\circ$), the γ -ray intensity follows closely the column density. This region is the *thin-target* regime, in which the attenuation of γ -rays is not important yet and the intensity scales directly with the amount of atmosphere for the proton-air interaction. For column densities larger

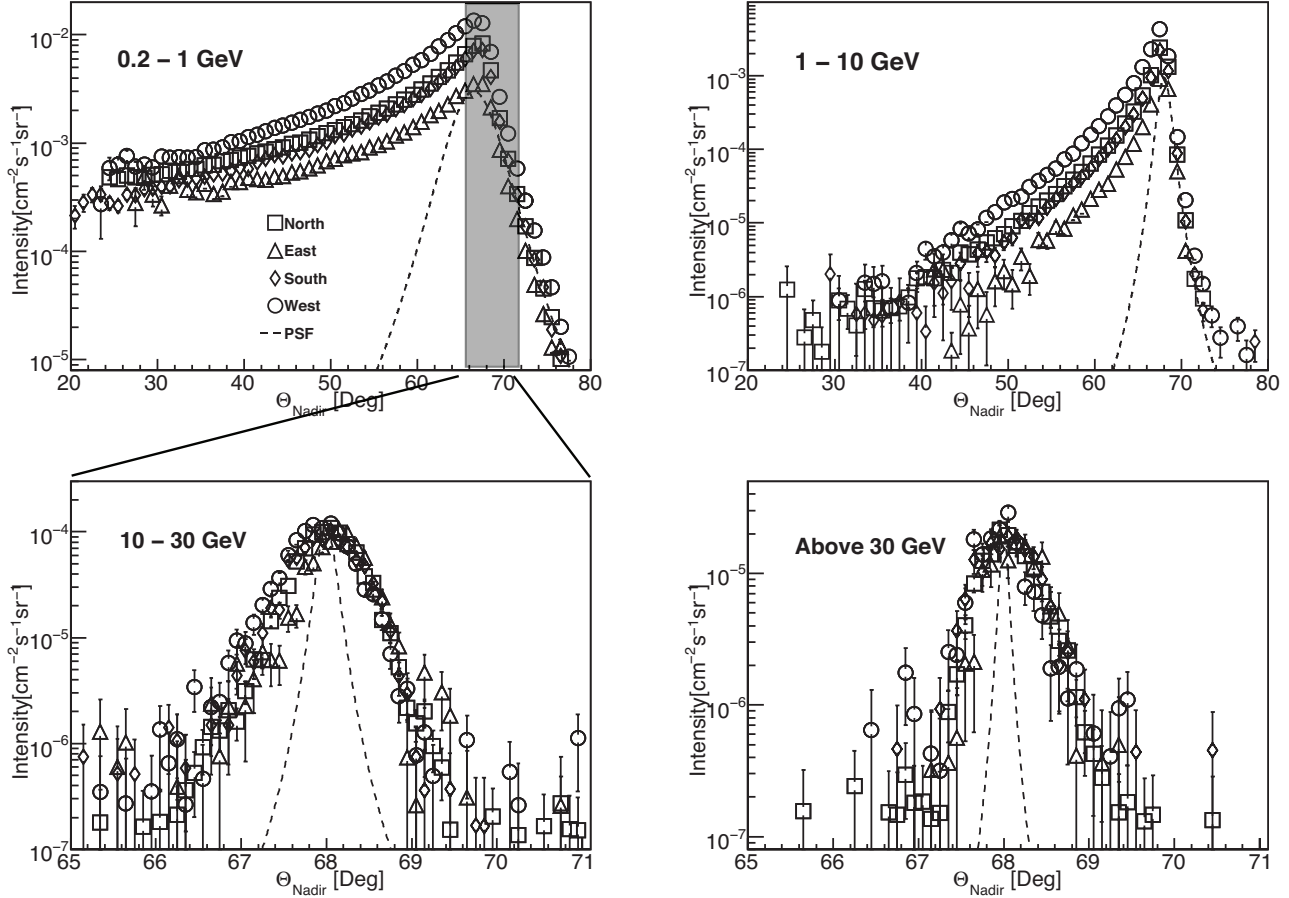


FIG. 4: Average intensity as a function of nadir angle in wedges towards the different directions (north, west, south, east) for 4 different energy bands. The narrowing of the emission with increasing energy is seen as well as the change in shape (with a broad tail towards the center of the Earth for low energies) and a very narrow limb for the high energies. The comparison of the PSF calculated for the lower bound of the energy bin (averaged between front and back-converting events) is shown as a dashed line. Note that the range of the histogram and the binning is different for the two high-energy bands.

than $\sim 10 \text{ g cm}^{-2}$ the atmosphere starts to be optically thick for γ -rays and absorption (i.e. a deviation from the scaling with density) sets in.

If the target is thin enough that the secondary γ -rays are practically not attenuated, the observed γ -ray intensity should have a power-law index close to the index of ambient cosmic rays. Indeed, it has been shown that the assumption of a constant fraction $\kappa \sim 0.17$ of energy of the incident proton released in the secondary γ -rays (δ -function approximation) works well in proton-proton interactions for $1 \text{ GeV} \lesssim E_\gamma \lesssim 100 \text{ GeV}$ [19, 24]. The Earth's atmosphere consists predominantly of N and O, and there is a significant fraction of He in cosmic rays. This difference in the beam and target composition could be taken into account by introducing an approximate energy independent correction factor, but we are currently interested in the spectral slope and not in the absolute normalization of the γ -ray intensity. Therefore, a comparison of the ambient spectrum of protons, with the energy scaled by a factor of κ , with the observed spectrum of γ -rays may be used to check the equality of their spectral indices and to test the energy calibration of the LAT instrument.

Figure 6 shows the γ -ray spectrum for the optically thin region ($68.6^\circ < \Theta_{\text{nadir}} < 69.6^\circ$) compared to the proton spectrum with the energy scaled by a factor of κ . The proton intensity is scaled by first scaling the energy of each intensity point by a factor κ , and then re-normalizing the resulting proton intensity down by 0.7. In this way the proton intensity matches the γ -ray intensity at 1 GeV (i.e., the ratio is normalized to unity at 1 GeV). The general good agreement is further demonstrated by the inset in Figure 6 which shows the ratio of the γ -ray intensity to the scaled proton intensity.

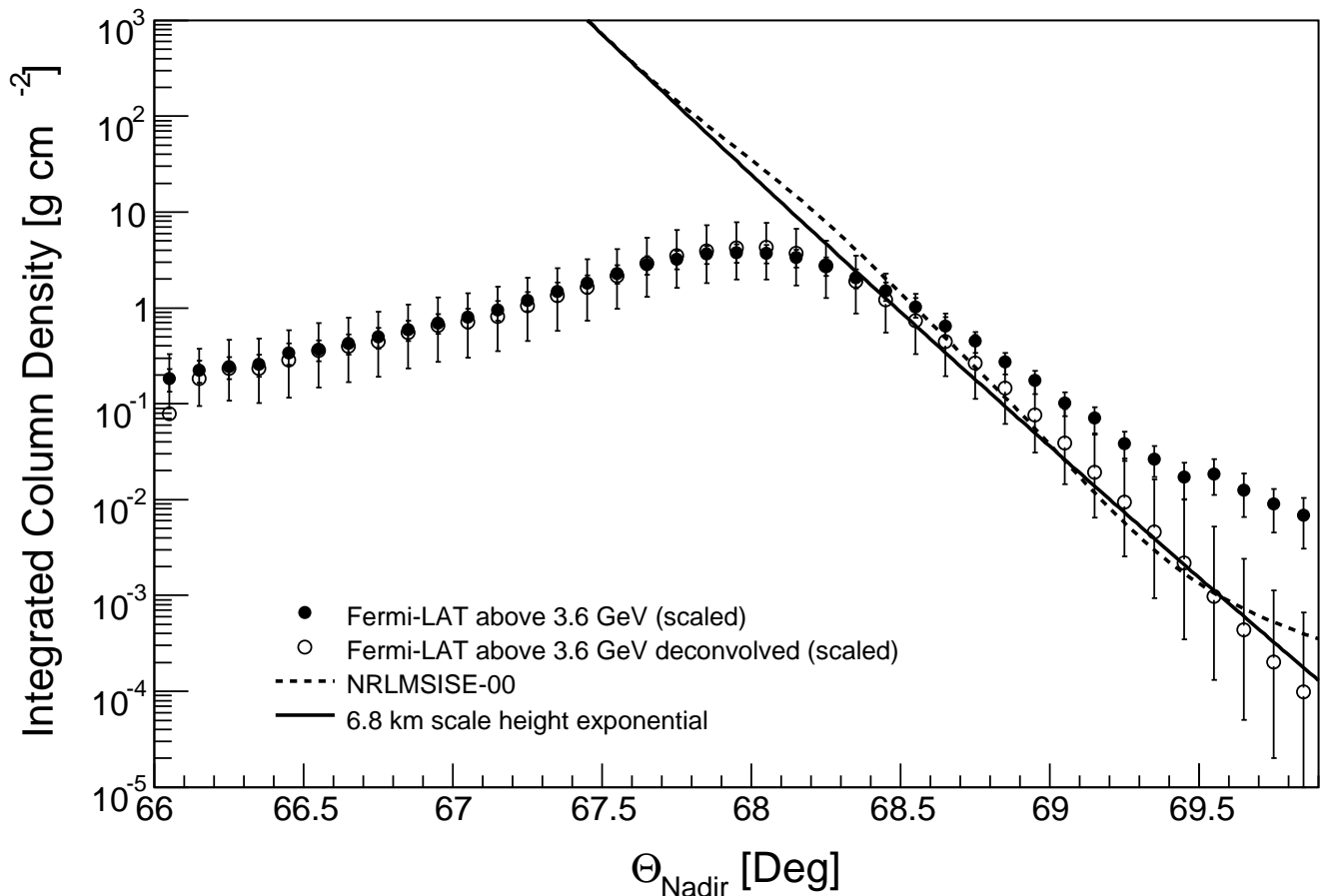


FIG. 5: Comparison between the integrated column density with the LAT-detected gamma-ray intensity as a function of nadir angle for events above 3.6 GeV. Two different model atmospheric profiles have been used: a simple barometric atmosphere with scale height of 6.8 km [22] shown as solid line and a more realistic atmospheric model from [23]. Shown are the measured gamma-ray intensity (solid circles) and the gamma-ray intensity deconvolved by the PSF of the median energy (4.7 GeV) of this data set (open circles). A good correspondence between the γ -ray intensity and the column density can be seen at angles $\Theta_{\text{Nadir}} \gtrsim 68.3^\circ$. For these angles the atmosphere is thin enough (column density $< 10 \text{ g cm}^{-2}$) so that no significant attenuation occurs and the γ -rays are directly related to the amount of target material for the incoming cosmic rays. The absolute level of the γ -ray intensity has been scaled to match the column density for the barometric atmosphere model.

IV. CONCLUSION

Data from the LAT have been used to study the γ -ray emission generated in the interactions of cosmic rays with the Earth's atmosphere for over more than four orders of magnitude between 100 MeV and 1 TeV with unprecedented precision. The data set contains 218 photons above 100 GeV, and 16 photons above 500 GeV. These measurements therefore demonstrate the capability of the LAT to detect and determine energies for photons up to TeV energies. Two-dimensional intensity maps as well as azimuthal and zenithal profiles and energy spectra of the Earth albedo emission have been derived which show several effects:

- A bright limb at the Earth's horizon. These limb γ -rays are dominantly generated by grazing-incidence cosmic-ray showers coming directly towards the LAT. The γ -ray spectral index follows the spectral index of the incident cosmic ray spectrum in the limb region up to γ -ray energies of $E \gg 100 \text{ GeV}$.
- A soft-spectrum nadir region dominated by γ -rays back-scattered at large angles originating from cosmic-ray showers developing deep into the atmosphere. Due to increasing collimation of secondary particles with increasing energies, these γ -rays show a much softer spectrum.
- An east-west modulation for energies below $\sim 10 \text{ GeV}$, caused by the deflection of primary cosmic rays in Earth's magnetic field. Higher energy cosmic rays are less affected by the magnetic field, resulting in a fading

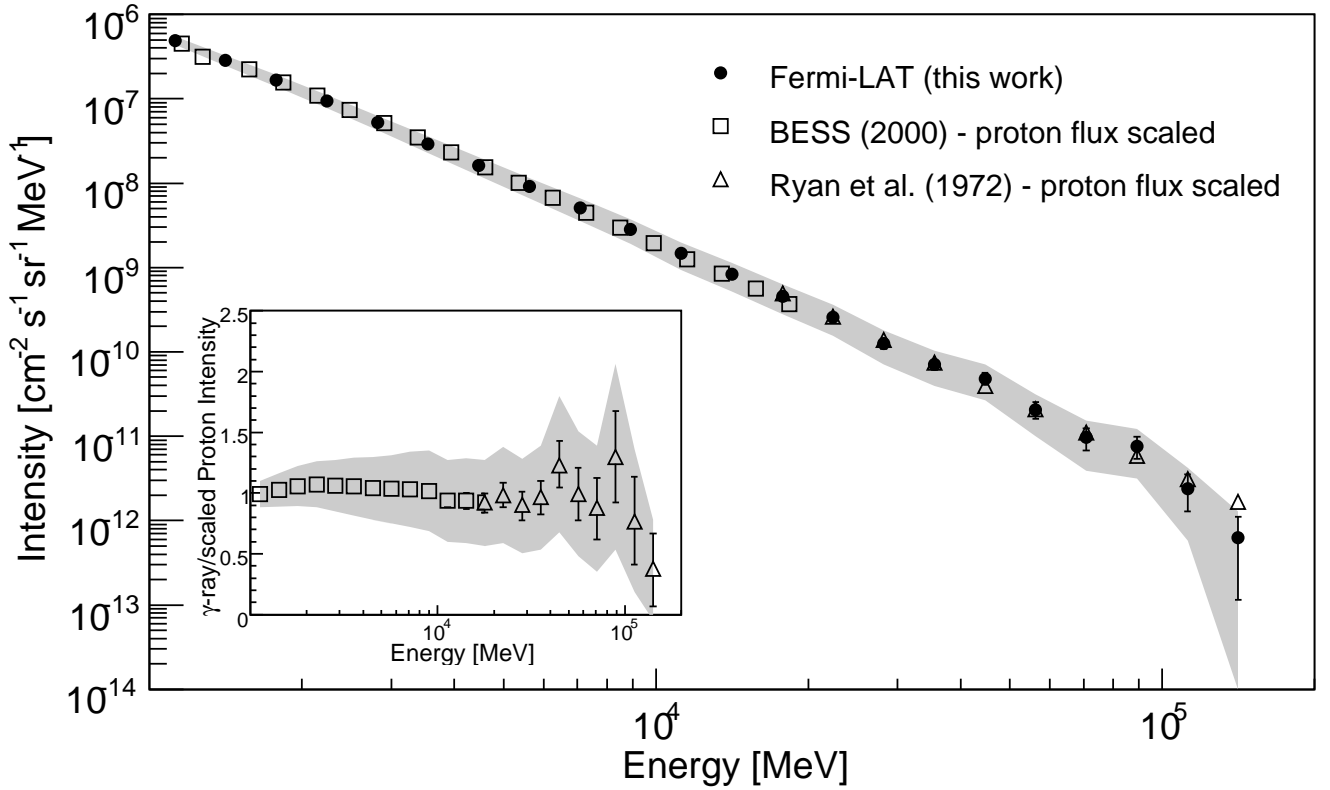


FIG. 6: A comparison of the measured gamma-ray intensity for the angular interval $68.6^\circ < \Theta_{\text{nadir}} < 69.6^\circ$ (thin target case, gamma-ray attenuation is insignificant) with the scaled cosmic ray proton intensity (see text for details). The inset shows the ratio between the γ -ray data and the scaled proton data and shows the general good match between the two measurements. The data have been taken from Sanuki et al. [18] and Ryan et al. [17].

modulation with increasing energy. The north-south ratio is equal to 1 within errors.

Figure 7 shows a compilation of photons generated in the atmosphere of the Earth in the energy range between 10 keV and 1 TeV. A direct comparison of the measurements from different instruments is not straightforward, since different instruments are integrating over different regions of the Earth. Also, the measurements have been taken at different times during the solar cycle and therefore correspond to different levels of solar modulation of the primary cosmic rays. The peak of the Earth γ -ray albedo energy flux is in the LAT range (for the limb, but potentially also when averaging over the whole Earth). The position of this peak can be understood from the power-law index of the cosmic-ray spectrum and the fact that neutral pion production is the dominant process. It is similarly visible in the spectrum of the diffuse Galactic emission [30]. Evident in Figure 7 is the huge energy range over which the LAT can make spectral measurements.

The LAT data provide a picture of the γ -ray emission from the Earth's atmosphere unprecedented in energy range, resolution and statistical precision. The data can be used to understand and model the interaction of cosmic rays in Earth's atmosphere and magnetic field. Since the Earth is such a bright source for the LAT, these data also provide valuable information for γ -ray background studies and can eventually be used as a calibration source.

Acknowledgments

The *Fermi* LAT Collaboration acknowledges generous ongoing support from a number of agencies and institutes that have supported both the development and the operation of the LAT as well as scientific data analysis. These include the National Aeronautics and Space Administration and the Department of Energy in the United States, the Commissariat à l'Énergie Atomique and the Centre National de la Recherche Scientifique / Institut National de Physique Nucléaire et de Physique des Particules in France, the Agenzia Spaziale Italiana and the Istituto Nazionale di

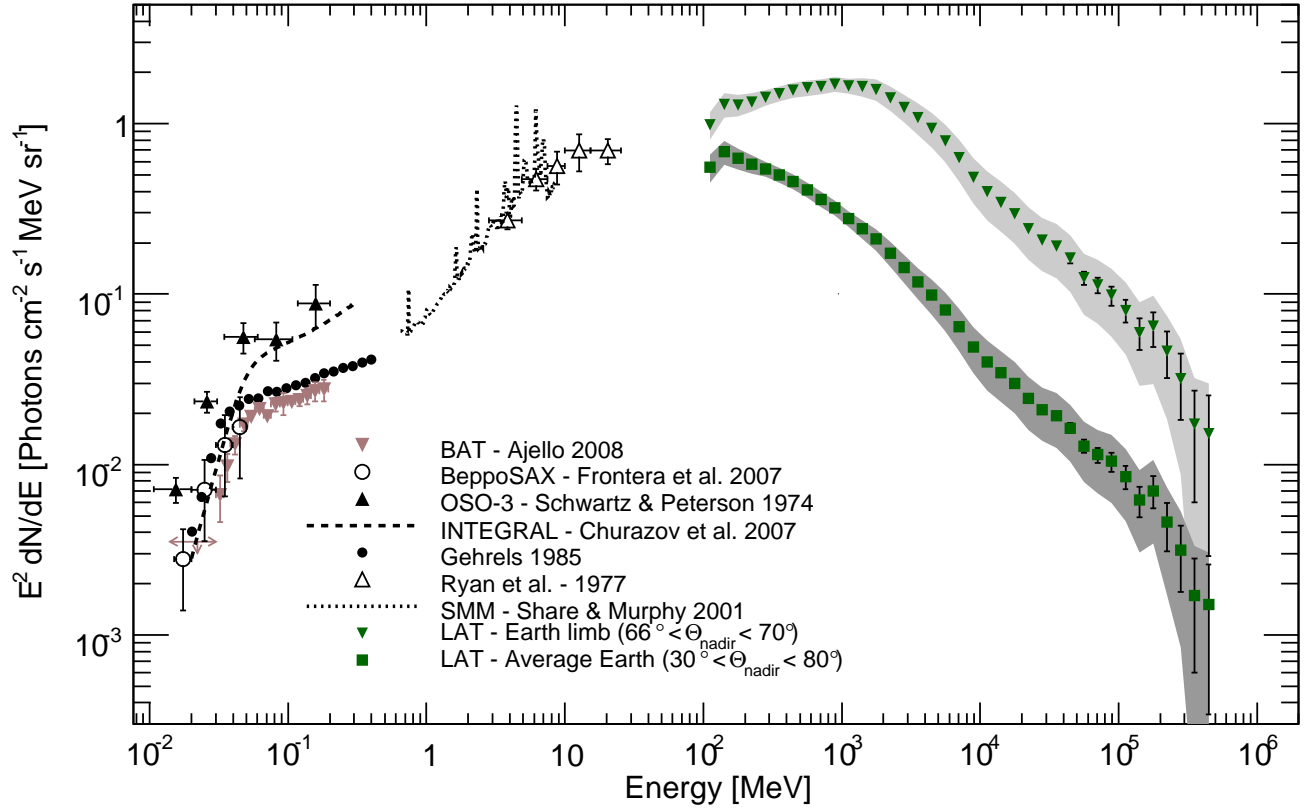


FIG. 7: Energy intensity for the Earth-originating γ -rays from keV to 500 GeV energies. The measurements from different instruments are not readily comparable since they have been taken in different points in the solar cycle and are also integrated over different areas of the Earth. Data points are taken from Ryan et al. [7], Share and Murphy [12], Ajello et al. [25], Frontera et al. [26], Schwartz and Peterson [27], Churazov et al. [28], Gehrels [29].

Fisica Nucleare in Italy, the Ministry of Education, Culture, Sports, Science and Technology (MEXT), High Energy Accelerator Research Organization (KEK) and Japan Aerospace Exploration Agency (JAXA) in Japan, and the K. A. Wallenberg Foundation, the Swedish Research Council and the Swedish National Space Board in Sweden.

Additional support for science analysis during the operations phase is gratefully acknowledged from the Istituto Nazionale di Astrofisica in Italy and the Centre National d'Études Spatiales in France.

-
- [1] D. J. Morris, *J. Geophys. Res.* **89**, 10685 (1984).
 - [2] F. W. Stecker, *Nature (London)* **242**, 59 (1973).
 - [3] W. L. Kraushaar, G. W. Clark, G. P. Garmire, R. Borken, P. Higbie, V. Leong, and T. Thorsos, *Astrophys. J.* **177**, 341 (1972).
 - [4] C. E. Fichtel, D. A. Kniffen, and H. B. Ögelman, *Astrophys. J.* **158**, 193 (1969).
 - [5] R. L. Kinzer, G. H. Share, and N. Seeman, *J. Geophys. Res.* **79**, 4567 (1974).
 - [6] G. J. Fishman, J. W. Watts, Jr., and C. A. Meegan, *J. Geophys. Res.* **81**, 6121 (1976).
 - [7] J. M. Ryan, S. H. Moon, R. B. Wilson, A. D. Zych, R. S. White, and B. Dayton, *J. Geophys. Res.* **82**, 3593 (1977).
 - [8] V. Schoenfelder, U. Graser, and J. Daugherty, *Astrophys. J.* **217**, 306 (1977).
 - [9] S. V. Golenetskii, I. A. Gurian, V. N. Ilinskii, E. P. Mazetz, and M. P. Proskura, *Geomagnetism and Aeronomy/Geomagnetizm i Aeronomiia* **15**, 203 (1975).
 - [10] W. L. Imhof, G. H. Nakano, and J. B. Reagan, *J. Geophys. Res.* **81**, 2835 (1976).
 - [11] I. A. Gurian, E. P. Mazets, M. P. Proskura, and I. A. Sokolov, *Geomagnetism and Aeronomy/Geomagnetizm i Aeronomiia* **19**, 11 (1979).
 - [12] G. H. Share and R. J. Murphy, *J. Geophys. Res.* **106**, 77 (2001).
 - [13] D. J. Thompson, G. A. Simpson, and M. E. Ozel, *J. Geophys. Res.* **86**, 1265 (1981).
 - [14] D. Petry, in *High Energy Gamma-Ray Astronomy*, edited by F. A. Aharonian, H. J. Völk, and D. Horns (2005), vol. 745

of *American Institute of Physics Conference Series*, pp. 709–714.

- [15] Fermi/LAT Collaboration: W. B. Atwood, *Astrophys. J.* **697**, 1071 (2009), 0902.1089.
- [16] A. A. Abdo, M. Ackermann, W. B. Atwood, R. Bagagli, L. Baldini, J. Ballet, D. L. Band, G. Barbiellini, M. G. Baring, J. Bartelt, et al., *Astrophys. J.* **696**, 1084 (2009), 0812.2960.
- [17] M. J. Ryan, J. F. Ormes, and V. K. Balasubrahmanyam, *Physical Review Letters* **28**, 985 (1972).
- [18] T. Sanuki, M. Motoki, H. Matsumoto, E. S. Seo, J. Z. Wang, K. Abe, K. Anraku, Y. Asaoka, M. Fujikawa, M. Imori, et al., *Astrophys. J.* **545**, 1135 (2000), arXiv:astro-ph/0002481.
- [19] F. A. Aharonian and A. M. Atoyan, *Astron. Astrophys.* **362**, 937 (2000), arXiv:astro-ph/0009009.
- [20] H. P. Wellisch and D. Axen, *Phys. Rev. C* **54**, 1329 (1996).
- [21] C. Amsler, M. Doser, M. Antonelli, D. Asner, K. Babu, H. Baer, H. Band, R. Barnett, E. Bergren, J. Beringer, et al., *Physics Letters B* **667**, 1 (2008), ISSN 0370-2693, review of Particle Physics.
- [22] T. K. Gaisser, *Cosmic rays and particle physics* (Cambridge Univ. Press, Cambridge, 1990).
- [23] J. M. Picone, A. E. Hedin, D. P. Drob, and A. C. Aikin, *Journal of Geophysical Research (Space Physics)* **107**, 1468 (2002).
- [24] S. R. Kelner, F. A. Aharonian, and V. V. Bugayov, *Phys. Rev. D* **74**, 16 (2006).
- [25] M. Ajello, J. Greiner, G. Sato, D. R. Willis, G. Kanbach, A. W. Strong, R. Diehl, G. Hasinger, N. Gehrels, C. B. Markwardt, et al., *Astrophys. J.* **689**, 666 (2008), 0808.3377.
- [26] F. Frontera, M. Orlandini, R. Landi, A. Comastri, F. Fiore, G. Setti, L. Amati, E. Costa, N. Masetti, and E. Palazzi, *Astrophys. J.* **666**, 86 (2007), arXiv:astro-ph/0611228.
- [27] D. A. Schwartz and L. E. Peterson, *Astrophys. J.* **190**, 297 (1974).
- [28] E. Churazov, R. Sunyaev, M. Revnivtsev, S. Sazonov, S. Molkov, S. Grebenev, C. Winkler, A. Parmar, A. Bazzano, M. Falanga, et al., *A&A* **467**, 529 (2007), arXiv:astro-ph/0608250.
- [29] N. Gehrels, *Nuclear Instruments and Methods in Physics Research A* **239**, 324 (1985).
- [30] A. W. Strong, I. V. Moskalenko, and O. Reimer, *Astrophys. J.* **613**, 962 (2004), arXiv:astro-ph/0406254.